

Magnetohydrodynamic Simulations of Shock Interactions with Radiative Clouds

P. Chris Fragile¹, Peter Anninos¹, Kyle Gustafson², and Stephen D. Murray¹

ABSTRACT

We present results from two-dimensional numerical simulations of the interactions between magnetized shocks and radiative clouds. Our primary goal is to characterize the dynamical evolution of the shocked clouds. We perform runs in both the strong and weak magnetic field limits and consider three different field orientations. For the geometries considered, we generally find that magnetic fields external to, but concentrated near, the surface of the cloud suppress the growth of destructive hydrodynamic instabilities. External fields also increase the compression of the cloud by effectively acting as a confinement mechanism driven by the interstellar flow and local field stretching. This can have a dramatic effect on both the efficiency of radiative cooling, which tends to increase with increasing magnetic field strength, and on the size and distribution of condensed cooled fragments. In contrast, fields acting predominately internally to the cloud tend to resist compression, thereby inhibiting cooling. We observe that, even at modest strengths ($\beta_0 \lesssim 100$), internal fields can completely suppress low-temperature ($T < 100$ K) cooling.

Subject headings: hydrodynamics — ISM: clouds — ISM: kinematics and dynamics — magnetic fields — MHD — shock waves

1. Introduction

Shock waves are an important and common feature in both interstellar (ISM) and intergalactic (IGM) media. They are triggered by such energetic phenomena as jets, supernovas, cloud-cloud collisions, and stellar winds and provide a means for transferring energy from such events into the ambient gas. Since the ISM and IGM are generally inhomogeneous, an important problem in astrophysics is understanding the interaction of these shocks with overdense clumps or clouds. A thorough review of this problem in the unmagnetized and non-radiative limits is provided by Klein et al. (1994).

Of special interest to us is large-scale shock-induced star formation, particularly in the neighborhoods of extragalactic radio jets. One of the first objects demonstrated to show a correlation between a radio jet and regions of active star formation was the nearest radio galaxy, Centaurus A (e.g. Blanco et al. 1975). Other examples have been found as the sensitivity and spatial resolution of radio and optical telescopes has improved. For instance, “Minkowski’s Object” is a peculiar small starburst system at the end of a radio jet emanating from the elliptical galaxy NGC 541, located near the center of the cluster of galaxies Abell 194 (van Breugel et al. 1985). Correlations between radio and optical emissions have also been observed in the so-called “alignment effect” in distant ($z > 0.6$) radio galaxies (Chambers et al. 1987; McCarthy et al. 1987).

These observations are most convincingly explained by models in which shocks generated by the radio jet propagate through an inhomogeneous medium and trigger gravitational collapse in relatively overdense

¹University of California, Lawrence Livermore National Laboratory, Livermore, CA 94550

²Department of Physics, University of Missouri - Columbia, Columbia, MO 65201

regions, leading to a burst of star formation (Begelman & Cioffi 1989; De Young 1989; Rees 1989). In a recent study (Fragile et al. 2004), we investigated a key component of such models - the radiative shock-induced collapse of intergalactic clouds. For moderate cloud densities ($\gtrsim 1 \text{ cm}^{-3}$) and shock Mach numbers ($\lesssim 20$), we found that cooling processes can be highly efficient and result in more than 50% of the initial cloud mass cooling to below 100 K. The cold, dense fragments that form are presumably the precursors to active star-forming regions.

In the current work we consider the effects of dynamically important magnetic fields in radiative shock-cloud collisions. Magnetic fields are known to be a pervasive element of the ISM and IGM and are often relevant in characterizing the local and global dynamical behaviors of these media. In shock-cloud interactions, magnetic fields can act to suppress destructive hydrodynamic instabilities by providing additional tension at the interface between the cloud and the post-shock background gas (Nittman 1981; Mac Low et al. 1994). Magnetic fields can also limit the growth of disruptive vortices that form in the wake of the cloud, again primarily due to tension in the magnetic field lines as they are wound up within the vortices. Strong external magnetic fields can also increase the compression of the shocked cloud material, due to the increased external magnetic pressure. This compression enhances the radiative efficiency of the cloud and allows additional cooling beyond that achievable without magnetic fields. However, strong internal magnetic fields can resist compression, thereby inhibiting cooling of the cloud. In this paper we explore these competing effects and the general role of magnetic fields in radiative shock-cloud collisions. This paper also reports on the addition of magnetic fields to our astrophysical hydrodynamics code, *Cosmos*. We proceed in §2 by describing the models considered in this work. In §3 we describe our implementation of radiation MHD. Our results are presented in §4 and discussed further in §5.

2. Models

Models of shock-induced star formation are generally built upon the assumption of an inhomogeneous two-phase medium consisting of warm or cold dense clouds or clumps embedded in a hot, tenuous background medium. Following Rees (1989), Begelman & Cioffi (1989), and McCarthy (1993), we assume a background temperature $T_{b,i} = 10^7 \text{ K}$ and density $n_{b,i} = 0.01 \text{ cm}^{-3}$. In this work we restrict ourselves to modeling isolated clouds. Each cloud has an initial temperature $T_{cl,i} = 10^4 \text{ K}$, appropriate for warm, ionized gas. Assuming pressure equilibrium between the two phases, the density of the cloud is $n_{cl,i} = (T_{b,i}/T_{cl,i})n_{b,i} = \chi n_{b,i} = 10 \text{ cm}^{-3}$, where $\chi = 10^3$ is the density ratio between the cloud and background gases. A planar shock of velocity $v_{sh,b} = 3.7 \times 10^3 \text{ km s}^{-1}$ ($\mathcal{M} = 10$, where \mathcal{M} is the Mach number, measured in the background gas) is set up to propagate across this cloud. This background shock triggers a secondary, compressive shock of velocity

$$v_{sh,cl} \simeq \left(\frac{n_{b,i}}{n_{cl,i}} \right)^{1/2} v_{sh,b} = \frac{v_{sh,b}}{\chi^{1/2}}. \quad (1)$$

inside the cloud.

We require the clouds in these models to be large enough not to be destroyed by the shock prior to the onset of cooling. This is equivalent to requiring $t_{cool} \ll t_{cc}$ or $q_s = \lambda_{cool}/R_{cl} \ll 1$, where

$$t_{cool} \approx \frac{1.5k_B T_{cl,ps}}{(n_{cl,ps})\Lambda(T)} \quad (2)$$

is the cooling time,

$$t_{cc} = \frac{R_{cl}}{v_{sh,cl}} \simeq \chi^{1/2} \frac{R_{cl}}{v_{sh,b}}, \quad (3)$$

is the cloud-compression or cloud-destruction timescale, q_s is the cooling parameter, and $\lambda_{cool} \approx v_{sh,cl} t_{cool}$ is the cooling length. Provided $t_{cool} \ll t_{cc}$ (or $q_s \ll 1$), the shock is radiative and the post-shock gas loses much of its internal energy during compression. If radiative losses significantly outpace compressive heating, an initial compressive shock can trigger cooling to very low temperatures (Mellema et al. 2002; Fragile et al. 2004). If, however, $t_{cool} > t_{cc}$ (or $q_s > 1$), the shock-heated gas does not have time to cool before it is diffused into the background gas (Klein et al. 1994). Approximating the cooling function as $\Lambda = 1.33 \times 10^{-19} T^{-1/2}$ erg cm³ s⁻¹ (Kahn 1976), the restriction on the cloud radius becomes

$$\left(\frac{R_{cl}}{100 \text{ pc}} \right) \gtrsim 1.2 \times 10^{-4} \left(\frac{\chi}{10^3} \right)^{-2} \left(\frac{v_{sh,b}}{10^3 \text{ km s}^{-1}} \right)^4 \left(\frac{n_{cl,i}}{1 \text{ cm}^{-3}} \right)^{-1}. \quad (4)$$

For the parameters used in this work, R_{cl} needs only to be larger than about 0.2 pc ($\lambda_{cool} \approx 0.02$ pc). However, we choose $R_{cl} = 100$ pc in order to link our work with previous unmagnetized radiative shock-cloud simulations [run A in Mellema et al. (2002) and model E3 in Fragile et al. (2004)]. The larger cloud is also more reasonable for triggering a large burst of star-formation. All of the cooling runs in this work therefore begin with $q_s \approx 2 \times 10^{-4}$, $t_{cool} = 190$ yr, and $t_{cc} = 0.85$ Myr.

In this work we consider an array of simulations in the strong and weak magnetic field limits. We include runs with initial field strengths of $\beta_0 = 1, 4, 100$, and ∞ , where $\beta = P/(B^2/8\pi)$ is the ratio of hydrodynamic to magnetic pressure in the pre-shock region. Although magnetic field strengths are difficult to measure in astrophysics, β appears to be of order 10 in the diffuse regions of the ISM (Mac Low & Klessen 2004). A value of $\beta_0 = 4$ in our models corresponds to an initial field strength in the pre-shock region of 9.3 μG , comparable to inferred interstellar field strengths (Rand & Kulkarni 1989; Fitt & Alexander 1993). As in Fragile et al. (2004), our models are two-dimensional, in Cartesian geometry. In this geometry, we consider three different field orientations: (1) parallel to both the planar shock front and the cylindrical cloud (B_z), (2) parallel to the shock front but perpendicular to the cloud (B_y), and (3) perpendicular to the shock front and the cloud (B_x). For the strong shocks considered here, B_z and B_y are enhanced by about a factor of $(\gamma + 1)/(\gamma - 1) = 4$ (for a $\gamma = 5/3$ gas) in the post-shock region, whereas B_x is continuous across the shock. We also consider runs with and without radiative cooling active for each of the field orientations. Together, these runs facilitate an easy comparison of results with various magnetic field configurations and atomic processes using a single numerical scheme. The various runs and physical parameters of each shock-cloud simulation considered in this study are summarized in Table 1.

For the strong magnetic field cases we distinguish between what we consider primarily *internal* fields (B_z component) and what we consider primarily *external* fields (B_x and B_y components), differentiated by the regions where their effects are greatest. We make this distinction based upon the fact that the B_z field component, being parallel to the cylindrical cloud, plays no role other than to modify the total effective pressure (there are no gradients in the z -direction, so the $\mathbf{B} \cdot \nabla$ terms in equations (10) and (12) below drop out). However, for the strong shocks considered here, the post-shock gas pressure is generally much higher than the magnetic pressure, $(P/[B^2/8\pi] = \beta \approx 2\gamma[\gamma - 1]^2/[\gamma + 1]^3 \mathcal{M}^2 \beta_0 \gg 1)$, and so the B_z component plays little role in the non-radiative case (Jones et al. 1996). For a strongly radiating shock, however, the thermal gas pressure can drop quite dramatically behind the shock. Magnetic pressure can then become dominant in the post-shock layer and prevent further compression once $B_{z,cl}^2/8\pi = \rho_{cl,i} v_{sh,cl}^2$ (McKee & Hollenbach 1980) or

$$\left(\frac{\rho_{max}}{\rho_{cl,i}} \right) = \left(\frac{\mu m_H v_{sh,b}^2 \beta_0}{k_B T_{b,i}} \right)^{1/2}. \quad (5)$$

Prior to this, the cooling will proceed approximately isobarically. After this, any further cooling may only proceed approximately isochorically. For our usual parameters, with $\beta_0 = 4$, this predicts a peak density

enhancement of $\rho_{max}/\rho_{cl,i} \approx 26$. The field amplification B_{max}/B_i *inside* the cloud should be identical. If we now assume the cloud compresses isothermally due to radiative cooling, then we can estimate β inside the cloud since both the thermal gas pressure and magnetic field strength scale directly with density in this case. Thus, $\beta = P/(B^2/8\pi) \propto \rho^{-1}$ inside the cloud. The actual equation of state in our radiatively cooled runs is much softer than $P \propto \rho$, so this line of reasoning only implies an upper limit $\beta_{min} < (\rho_{cl,i}/\rho_{max})\beta_0$. We emphasize that this analysis strictly applies only to our radiatively-cooled B_z runs.

As the dominant role of the B_z field is restricted to the interior of the cloud, we consider it an internal field. On the other hand, we refer to B_y and B_x components as external fields. This does *not* mean that these field lines do not penetrate the cloud or have no role in the cloud interior. Rather it refers to the fact that their dominant roles are along the cloud surface or even external to the cloud. In fact, for our B_x cases, we do not expect much of a change from our unmagnetized results because the shock proceeds mostly parallel to the field lines, preventing the Lorentz force from acting. The magnetic fields, therefore, are not able to feed back strongly on the hydrodynamic evolution. In our B_y cases, on the other hand, the fields have a dominant role in the cloud evolution. These fields become trapped at the nose of the cloud allowing the magnetic pressure and field tension to continually increase, at least until the cloud is accelerated to the velocity of the post-shock flow. We can get a rough estimate of when this will occur by considering just the Lorentz acceleration term, which for the cloud is approximately $B_{y,i}^2/(4\pi\rho_{b,i}R_{cl})$. Assuming a constant acceleration, the velocity of the cloud will match that of the post-shock background gas after

$$t \approx \frac{3\mu m_H v_{sh,b} R_{cl} \beta_0}{8k_B T_{b,i}} , \quad (6)$$

where we have used the shock-jump condition $v_{b,ps} = 3v_{sh,b}/4$ for a $\gamma = 5/3$ gas. Using our normal parameters and $\beta_0 = 4$, we expect it will take the cloud approximately 6.4 Myr to reach the velocity of the post-shock background gas or about $8t_{cc}$.

We should note that our classification of field geometries as *internal* or *external* is particular to the two-dimensional Cartesian grid used in this work. For instance, if our cloud were a three-dimensional sphere, there would be no distinction between our B_y and B_z cases. Nevertheless, the contrast between internal and external field effects should remain valid even in three-dimensions. Realistically, magnetized shock-cloud collisions in nature will probably contain aspects of each of our idealized runs.

For runs in which radiative cooling is ignored, Klein et al. (1994) showed that the hydrodynamic shock-cloud problem is invariant under the scaling

$$t \rightarrow t\mathcal{M} , \quad v \rightarrow v/\mathcal{M} , \quad P \rightarrow P/\mathcal{M}^2 , \quad (7)$$

with distance, density, and pre-shock pressure left unchanged, provided $\mathcal{M} \gg 1$. Mac Low et al. (1994) showed that the non-radiative magnetohydrodynamic case obeys the same scaling relations provided

$$\mathbf{B} \rightarrow \mathbf{B}/\mathcal{M} . \quad (8)$$

Therefore, our non-radiative results are representative of *all* such cases provided $\mathcal{M} \gg 1$. However, these scaling relations do not hold when radiative cooling is important. For radiative clouds, the results depend sensitively on the initial parameters (Fragile et al. 2004).

3. Numerical Methods

We carry out our simulations using *Cosmos*, a massively parallel, multi-dimensional, multi-physics magnetohydrodynamic code for both Newtonian and relativistic flows developed at Lawrence Livermore National Laboratory. The relativistic capabilities and tests of *Cosmos* are discussed in Anninos & Fragile (2003). Tests of the Newtonian hydrodynamics options and of the microphysics relevant to the current work are presented in Anninos et al. (2003) and will not be discussed in detail here. The new elements introduced in this paper are the magnetic fields and their coupling to the fluid motion and state. Currently the magnetic fields are only implemented as part of the zone-centered and staggered-mesh artificial viscosity hydrodynamic schemes in *Cosmos*. The results in this paper use the zone-centered scheme. As this is the first work to introduce magnetic fields into *Cosmos*, we discuss briefly the dynamical equations, reconnection corrections, divergence cleansing, and numerical tests.

The magneto-hydrodynamics (MHD) equations solved in *Cosmos* take the form:

$$\frac{\partial \rho}{\partial t} + \nabla \cdot (\mathbf{v}\rho) = 0, \quad (9)$$

$$\frac{\partial(\rho\mathbf{v})}{\partial t} + \nabla \cdot (\mathbf{v}\rho\mathbf{v}) = -\nabla \left(P + \frac{B^2}{8\pi} \right) + \frac{1}{4\pi}(\mathbf{B} \cdot \nabla)\mathbf{B} - \rho\nabla\phi, \quad (10)$$

$$\frac{\partial e}{\partial t} + \nabla \cdot (\mathbf{v}e) = -P\nabla \cdot \mathbf{v} + \frac{\eta}{4\pi}(\nabla \times \mathbf{B})^2 + \Lambda(T, \rho), \quad (11)$$

$$\frac{\partial \mathbf{B}}{\partial t} + \nabla \cdot (\mathbf{v}\mathbf{B}) = (\mathbf{B} \cdot \nabla)\mathbf{v} - \nabla \times (\eta\nabla \times \mathbf{B}) - \nabla\psi, \quad (12)$$

where \mathbf{v} is the fluid velocity, e is the fluid internal energy density, ρ is the fluid density, P is the fluid pressure, \mathbf{B} is the magnetic field, and ϕ is the gravitational potential obtained from Poisson's equation $\nabla^2\phi = 4\pi G\rho$. In practice, we ignore self gravity for the two-dimensional results presented here but include it in the equations in anticipation of future three-dimensional simulations of radiative magnetized shock-cloud collisions. The cooling function $\Lambda(T, \rho)$ is solved using the equilibrium cooling curve model described in previous work (Anninos et al. 2003; Fragile et al. 2004). This form of the MHD equations is derived with the standard assumptions relevant for many astrophysical problems: the system is nonrelativistic and fully ionized, the displacement currents in Maxwell's equations are neglected, the net electric charge is small, and the characteristic length scales are large compared to particle gyroradii scales.

In equations (11) and (12), η is the non-ideal resistivity coefficient, used here to correct for magnetic reconnection errors that can occur in numerical schemes that solve the internal (rather than total) energy equation (Magara et al. 1997; Stone & Pringle 2001). Artificial resistivity spreads current sheets out over a few zones to keep them resolved, and compensates partially for the energy lost in unresolved reconnection flows. This procedure is similar to the treatment of shocks in artificial viscosity schemes. We expect that such anomalous reconnection could be important for the flows considered here. Most of the results in this paper use the Stone & Pringle (2001) form of η

$$\eta_{SP} = \frac{k_1(\Delta x)^2}{\sqrt{4\pi\rho}} |\nabla \times \mathbf{B}|, \quad (13)$$

where Δx is the grid spacing and k_1 is a dimensionless parameter used to adjust the strength of the artificial

resistivity. By making the artificial resistivity proportional to $\nabla \times \mathbf{B}$, this form ensures that it has negligible effect in smooth regions of the flow, yet is large inside current sheets. However, we find that the simpler Nitta et al. (2001) form

$$\eta_N = k_1 v_A \Delta x , \quad (14)$$

where $v_A = B/\sqrt{4\pi\rho}$ is the Alfvén wave velocity, yields better results for the class of Riemann problems discussed in Falte (2002) (see Appendix A). For comparison, we present results of magnetized shock-cloud interactions using both forms of η , as well as a run without artificial resistivity.

The scalar potential ψ in equation (12) is introduced as a divergence cleanser to maintain a divergence-free magnetic field ($\nabla \cdot \mathbf{B} = 0$). Options are included in Cosmos to solve any one of the following constraint equations for ψ (Dedner et al. 2002):

$$\nabla^2 \psi = -\frac{\partial \nabla \cdot \mathbf{B}}{\partial t} \approx -\frac{\nabla \cdot \mathbf{B}}{\Delta t}, \quad (15)$$

$$\psi = -c_p^2 \nabla \cdot \mathbf{B}, \quad (16)$$

$$\frac{\partial \psi}{\partial t} = -\frac{c_h^2}{c_p^2} \psi - c_h^2 \nabla \cdot \mathbf{B}, \quad (17)$$

which correspond, respectively, to elliptic, parabolic, and mixed hyperbolic and parabolic constraints. Here c_p and c_h are user-specified constants used to regulate the filtering process and weight the relative significance of the hyperbolic and parabolic components. For all of the calculations presented in this paper, we use the strictly parabolic form, which we find to be the most effective and least costly method to preserve the divergence constraint. However, we have confirmed that its use makes relatively little difference in the dynamical evolution of the shocked clouds presented in the main body of this work. This is likely a result of adopting the nonconservative form of the MHD equations in which the acceleration terms proportional to $\nabla \cdot \mathbf{B}$ have been explicitly eliminated from equations (9) - (12) (Brackbill & Barnes 1980).

We have validated the newly added magnetic field equations using a standard set of single and multi-dimensional MHD tests including: advection of a localized pulse of transverse magnetic field, propagation of circularly polarized Alfvén waves, propagation of sheared Alfvén waves, magnetosonic rarefaction waves, multiple MHD Riemann problems, and an MHD shock-cloud collision problem. A brief summary of these test results is presented in the appendix of this paper.

The calculations in this work are carried out on a fixed, two-dimensional Cartesian (x,y) grid, implying that the simulated clouds are cylindrical rather than spherical. The computational grid is $8R_{cl} \times 8R_{cl}$ with the cloud initially located at the center of the grid. This is slightly larger than the grid we used in our previous work (Fragile et al. 2004). The larger grid allows us to maintain the leading edge of the bow shock on the grid. In tests we found about a 10% difference in some of the measured cloud parameters when comparing the smaller and larger grid, due primarily to the front edge of the bow shock reaching the inflow boundary of the smaller grid.

We use a constant inflow boundary condition for the post-shock gas along the left-most edge of the grid. The top and bottom boundaries use flat (zero-gradient) boundary conditions. The right boundary uses outflow ($v_x \geq 0$) conditions. For runs with zero magnetic field we employ a reflective boundary along the symmetry axis of the problem and only evolve half of the grid. As in our previous work we use a localized diffusion filter at all of the outflow boundaries to minimize strong reflections. We find that this technique does an adequate job of preventing unphysical feedback from the boundaries while maintaining the integrity of the interior solution.

Runs BY4C(L), BY4C(L1), and BY4C(L2) are carried out at a fixed spatial resolution of $\Delta x = \Delta y = 1$ pc. All of the remaining runs have twice that resolution ($\Delta x = \Delta y = 0.5$ pc). The higher resolution runs have 200 zones per cloud radius, a value well above the resolution requirements suggested by Klein et al. (1994) for non-radiative clouds. However, in the presence of cooling, which leads to extreme compressions and steep density gradients, the resolution requirement becomes more stringent. In general, we find that we are only able to reliably follow the fragmentation of the cloud for approximately one hydrodynamic cloud-compression timescale (equation 3). Beyond this time, further compression of the cloud is prevented by numerical resolution rather than any physical mechanism.

4. Results

Figure 1 shows density contour plots for runs A, C, BZ4A, BZ4C, BY4A, BY4C, BX4A, and BX4C at $t = t_{cc}$. Several conclusions are immediately obvious from this figure: As noted in previous studies (Mellema et al. 2002; Fragile et al. 2004), radiative cooling can have a critical effect on the evolution of shocked clouds; strong magnetic fields can also be dynamically important to the growth of instabilities and to the compression of the cloud (Mac Low et al. 1994; Jones et al. 1996; Gregori et al. 1999, 2000); depending upon its orientation, the magnetic field can either enhance or resist cloud compression, actions which strongly affect the cooling efficiency of the cloud.

In the following sections we present more detailed analysis of our results as follows: In §4.1 we consider the role of hydrodynamic instabilities; in §4.2 we discuss the evolution of the magnetic fields, particularly their amplification; in §4.3 we quantify the compression of each model cloud, which is important to our discussion of cooling efficiency in §4.4. In §§4.5 and 4.6, we explore the role of initial field strength and numerical resolution, respectively, on our results. Finally, in §4.7, we discuss reconnection and the role of artificial resistivity.

4.1. Hydrodynamic Instabilities

Previous studies (Klein et al. 1994) have shown that strong shocks destroy unmagnetized, non-radiative clouds on a few dynamical timescales primarily through the growth of hydrodynamic (Kelvin-Helmholtz and Rayleigh-Taylor) instabilities. The early growth of these instabilities is clearly seen in Figure 1, particularly for run A (our non-radiative, unmagnetized case). These instabilities are seeded by the computational grid; hence, their nonlinear evolution is sensitive to the exact details of the simulation, including resolution and hydrodynamic method. For instance, we noticed differences in the precise structure of the clouds at late times when we compared staggered-mesh and zone-centered versions of our code at the same resolution. However, the important global characteristics of each simulation, such as field amplification, cloud compression, and cooling efficiency, are much less sensitive to these computational issues and we feel can therefore be reliably compared.

If the radiative efficiency of the gas has a sufficiently shallow dependence upon the temperature, then radiative emissions cool the gas rapidly, in a runaway process, producing even higher densities as the cooling gas attempts to re-attain pressure balance with the surrounding medium (Field 1965; Murray & Lin 1989). We find this can lead to an increase in the density contrast between the cloud and background of order $\gtrsim 10^3$ above that achieved in non-radiative cases, thus reducing the growth rate of the Kelvin-Helmholtz instability ($t_{KH}^{-1} = kv_{rel}/\chi^{1/2}$, Chandrasekhar 1961) by a factor $\gtrsim 30$. The slower growth rate helps stabilize the cloud

as seen, for instance, by comparing the results of run A (non-radiative, unmagnetized case) and C (radiative, unmagnetized case) in Figure 1.

Mac Low et al. (1994) and Jones et al. (1996) have shown numerically that predominantly external magnetic fields (combinations of B_x and B_y) are very efficient at suppressing hydrodynamic instabilities, primarily due to tension in the magnetic field lines maintaining a more laminar flow around the cloud surface. Linear theory (Chandrasekhar 1961) predicts Kelvin-Helmholtz instabilities will be suppressed if the local Alfvén speed exceeds roughly the velocity difference across the boundary, or $\beta < 2/\mathcal{M}^2$ for a $\gamma = 5/3$ gas. The Rayleigh-Taylor instability will be suppressed if the Alfvén crossing time is less than the acceleration timescale, or $\beta < (2/\gamma)(\chi/\mathcal{M})^2$. Thus, for the parameters chosen in this work ($\chi = 10^3$ and $\mathcal{M} = 10$), Rayleigh-Taylor growth is strongly suppressed in all the magnetized runs considered ($\beta < 10^4$), while Kelvin-Helmholtz is only suppressed in runs which evolve to a very strong field amplification ($\beta < 0.02$). These conclusions are consistent with the results observed in runs BY4A (non-radiative, B_y case) and BX4A (non-radiative, B_x case) compared to run A (non-radiative, unmagnetized case) in Figure 1.

The combined effect of strong external magnetic fields with cooling is to further suppress these instabilities. This is illustrated by runs BY4C and BX4C in Figure 1.

4.2. Field Amplification

Magnetic fields can generally be amplified in one of two ways: (1) squeezing of field lines through compression, or (2) stretching of field lines through sheared motion. For external fields, stretching is much more important than squeezing (Mac Low et al. 1994; Jones et al. 1996), whereas for internal fields, compression inside the cloud provides the greatest amplification, particularly for radiative clouds.

In Figure 2 we present grayscale contour plots of $\log(\beta)$ for runs BZ4A, BZ4C, BY4A, BY4C, BX4A, and BX4C. Also, in Table 2 we record the minimum value of β and the peak magnetic field enhancement (B_{max}/B_i) achieved in all simulations at $t = t_{cc}$.

For internal fields parallel to the cylindrical cloud (B_z), changes in the field strength simply follow changes in the density, as the fields are locked within the gas. Thus, the location of the greatest magnetic field amplification coincides with the location of peak density amplification, generally near colliding shocks inside the cloud. We therefore expect $B_{max}/B_i \geq \rho_{max}/\rho_{cl,i}$ for the B_z runs, with $B_{max}/B_i > \rho_{max}/\rho_{cl,i}$ only if the peak field amplification occurs in the background gas. For non-radiative clouds the high density regions are also regions of high gas pressure, so the magnetic pressure fails to dominate anywhere inside the cloud (see panel C of Figure 2). However, for radiative clouds, the highest density regions cool most efficiently and have thermal gas pressures significantly below the magnetic pressure. The magnetic fields thus provide an extra stiffness to such clouds relative to unmagnetized ones. Notice the dramatically smaller β_{min} in run BZ4C ($\beta_{min} = 1.9 \times 10^{-3}$) compared to BZ4A ($\beta_{min} = 4.1$), despite the fact that the peak magnetic field enhancement is somewhat comparable ($B_{max}/B_i = 73$ for run BZ4C and 13 for run BZ4A).

For external fields perpendicular to the direction of shock propagation (B_y), the greatest field amplification is at the front of the cloud. This is because the background flow continues to stretch field lines around the nose of the cloud. Since the clouds simulated here represent infinite cylinders, the field lines cannot “slip” around them as they might for a spherical cloud. The cloud is enveloped in an ever-thickening cocoon of magnetic field lines. Thus, even an initially small field can build up to become dynamically important (Jones et al. 1996). However, because most of the field amplification is external to the cloud, where radiative

cooling remains inefficient, β_{min} is not significantly different between the non-radiative (BY4A) and radiative (BY4C) runs (1.6×10^{-5} and 3.8×10^{-5} , respectively). The difference lies in the degree of cloud compression in the two runs due to runaway cooling in the radiative cloud. We will return to this point below.

The increased tension in the field lines also provides an extra acceleration force on the cloud. This explains the greater displacement of the clouds in runs BY4A and BY4C (relative to, say, runs BZ4A and BZ4C respectively) in Figure 1. In both cases, the cloud is accelerated to a velocity $v_{cl} \approx 120 \text{ km s}^{-1}$ at the end of the simulation. Amplification of the field will continue until the cloud is accelerated to a velocity matching the post-shock flow $v_{b,ps} \approx 2800 \text{ km s}^{-1}$.

For external fields parallel to the direction of shock propagation (B_x), the field lines initially anchored in the cloud play the biggest role in its evolution. The minimum value of β initially occurs near the symmetry plane downwind of the cloud, where a “flux tube” forms (Mac Low et al. 1994). This field enhancement is triggered by the rapid evacuation of gas from this region as a Mach stem forms in the shadow of the cloud. The field is also amplified by field stretching along the surface of the cloud and in vortices, primarily in the wake of the cloud. However, both of these forms of amplification result in oppositely directed fields becoming adjacent. This configuration is unstable to reconnection, so the net amplification is limited. Again, due to strong cooling in run BX4C, the thermal pressure inside the cloud drops significantly and allows the magnetic pressure to build up to a dynamically important value as evident in panel H of Figure 2.

4.3. Cloud Compression

One of our goals in this work is to quantify the efficiency of cloud compression for each of the runs. Previous authors (e.g. Jones et al. 1996) have tracked only the lateral expansion of the cloud. However, such analysis does not fully account for longitudinal effects. Here we define cloud compression as $\zeta = A_{cl}(t)/A_{cl}^0$, where A_{cl}^0 is the initial cross-sectional area of cloud material and $A_{cl}(t)$ is the subsequent cross-sectional area at time t . In order to track the two gas components (cloud and background), we use two tracer fluids (\mathcal{T}_{cl} and \mathcal{T}_b) which are passively advected in the same manner as the density. Throughout each calculation the distribution of \mathcal{T}_{cl} reflects the distribution of original cloud material. Numerically, the cloud compression is calculated as

$$\zeta = \frac{\sum_{i,j} \mathcal{T}_{cl}(i,j;t)/[\mathcal{T}_{cl}(i,j;t) + \mathcal{T}_b(i,j;t)] \Delta x_i \Delta y_j}{\sum_{i,j} \mathcal{T}_{cl}^0(i,j) \Delta x_i \Delta y_j}, \quad (18)$$

where $\mathcal{T}_{cl}/(\mathcal{T}_{cl} + \mathcal{T}_b)$ gives an estimate of the volume fraction of cloud material in a given cell and $\mathcal{T}_{cl}^0(i,j) = 1$ inside the initial cloud and zero elsewhere.

Figure 3 shows the cloud compression as a function of time for the non-radiative (A, BZ4A, BY4A, and BX4A) and the radiatively-cooled (C, BZ4C, BY4C, and BX4C) $\beta_0 = 4$ runs. In Table 2 we record the peak density enhancement ($\rho_{max}/\rho_{cl,i}$) at $t = t_{cc}$ for all runs. All of the clouds are initially compressed over a timescale $t \approx t_{cc}$. However, after the period of initial compression, the non-radiative clouds re-expand. This re-expansion phase leads to the cloud destruction phase as the growth of hydrodynamic instabilities is accelerated (Klein et al. 1994). However, re-expansion is generally suppressed for radiative clouds. In our simulations, the cross-sectional areas of these clouds continue to decrease until they reach a limit set by numerical resolution rather than any physical mechanism. The radiatively-cooled B_z case (run BZ4C) is an exception. Here the internal magnetic field resists compression (thus inhibiting cooling) and allows the cloud to re-expand, similar to the non-radiative cases. Again, this makes the clouds more susceptible to destructive hydrodynamic instabilities as apparent in Figure 1. As expected, we find that the peak density

in each of the B_z runs is about equal to the value set by equation (5).

For runs BY4A and BY4C, the external field lines become trapped at the front of the cloud. Because the clouds simulated here represent infinite cylinders, the field lines cannot “slip” around them as they might for a spherical cloud. As more field lines wrap around the cloud, the compression becomes stronger. The only direction the cloud is able to expand is in the direction of the original shock propagation, as occurs for run BY4A. The extra compression in run BY4C causes runaway cooling at the highest rates we have observed, and the diminishing cloud quickly reaches the limits of our resolution.

In runs BX4A and BX4C, the magnetic field lines play little role in governing the compression of the clouds. Compression in these runs proceeds very similarly to the equivalent unmagnetized runs (A and C, respectively).

4.4. Cooling Efficiency

As was shown by Mellema et al. (2002) and Fragile et al. (2004), the evolution of cooling-dominated clouds is quite different than that of non-radiative clouds. Rather than re-expanding and quickly diffusing into the background gas, the compressed cloud fragments into numerous dense, cold, compact filaments. These filaments survive for many dynamical timescales and presumably may be the precursors to active star-forming regions. Contrast, for instance, the results of run A (non-radiative, unmagnetized case) and C (radiative, unmagnetized case) in Figure 1 to see the importance of radiative cooling.

Here we attempt to quantify the efficiency of the cooling processes in runs C, BZ4C, BY4C, and BX4C, each of which included radiative cooling. The same tracer fluid T_{cl} used to track the compression above also allows us to quantify how much of the initial cloud material cools below certain threshold temperatures. Figure 4 shows the fraction of cloud material that cools below $T = 1000$ and $T = 100$ K as a function of time. The percentage of gas that cools to below 1000 K gives a strong upper limit to the percentage that might form stars, while, when well resolved, the amount that cools to below 100 K gives a more accurate measure. In Table 2 we also record the minimum temperature achieved in each model at $t = t_{cc}$.

We note from the results that the cooling process is generally extremely efficient throughout the cloud, although some differences are noted for the different field configurations. Since cooling efficiency is driven predominately by local gas density, runs such as BZ4C, in which the internal magnetic field lines stiffen the cloud and reduce the compression, cooling is not as efficient as in the fiducial unmagnetized run (C). At the other extreme, strong external magnetic fields, such as those in run BY4C, greatly enhance the cooling efficiency, triggering greater rates of runaway cooling. Finally, in run BX4C, since the field plays little role in enhancing or reducing compression, it also has little effect on the overall cooling efficiency.

4.5. Role of Initial Field Strength

Thus far the magnetic field discussion has focused primarily on the effects of field orientation. Now we explore the effects of varying the initial field strength. Our general $\beta_0 = 4$ case corresponds to a reasonable initial field strength in the pre-shock region of $9.3 \mu\text{G}$, comparable to inferred interstellar and intergalactic field strengths (Rand & Kulkarni 1989; Fitt & Alexander 1993). Nevertheless, astrophysical magnetic field strengths can vary by many orders of magnitude (Vallée 2003). In the neighborhood of radio jets, the field strengths may be at least an order of magnitude higher than what we have chosen (e.g. Krause & Löhr 2004).

Furthermore, the dynamical importance of the magnetic fields depends on the thermal gas pressure, which itself can vary by orders of magnitude. This suggests a very wide range of values of β are plausible. Limits on computational resources prevent us from presenting a complete parameter study of field strengths, but we can nevertheless identify some important limits with a reasonably small set of simulations.

For the internal field (B_z) case (BZ4C) with $\beta_0 = 4$, the added stiffness of the magnetic pressure prevents any cloud gas from cooling below 100 K. One can then ask, how strong must the initial field be in order to prevent cooling below our higher temperature threshold of 1000 K? Conversely one can ask, how weak does the initial field need to be in order not to significantly inhibit cooling over the timescales considered? To attempt to answer these questions, we consider two additional field strengths for B_z : $\beta_0 = 1$ (run BZ1C) and $\beta_0 = 100$ (run BZ100C). In Figure 5, we compare the cloud compression and cooling efficiencies for the various B_z runs. We see that for the $\beta_0 = 1$ case, low temperature cooling is almost completely suppressed; only a small amount of gas is able to cool below 1000 K. The cloud also begins to re-expand towards the end of the simulation, a behavior commonly seen in simulations of non-radiative clouds. For $\beta_0 = 100$, the cloud behaves similarly to an unmagnetized, radiative cloud, although we note that there is still no cooling below 100 K. However, as noted in our previous work (Fragile et al. 2004), this particular diagnostic is very sensitive to small changes in the simulations, especially spatial resolution, so its usefulness is somewhat limited.

For the $\beta_0 = 4$, B_y field case (BY4C), we find that the increased compression from the trapped field lines greatly increases the cooling efficiency over the timescales considered. One can then ask, how weak must such a field be in order to not dramatically enhance the compression and cooling over the same timescale? We therefore construct an additional B_y run with $\beta_0 = 100$ (BY100C). The cloud compression and cooling efficiencies for the different B_y runs are presented in Figure 6. As we can see, the $\beta_0 = 100$ case behaves similarly to an unmagnetized cloud over the timescale considered. Nevertheless, as the magnetic field lines continue to build up on the nose of the cloud, even this initially weak field will eventually play an important role in the cloud evolution, although over a longer timescale than the cloud compression time.

Finally, we find that the magnetic fields in the B_x case with $\beta_0 = 4$ (BX4C) have little effect on the compression or cooling of the cloud. It is worth considering whether a stronger initial field might change this conclusion. Therefore we consider a B_x run with $\beta_0 = 1$ (run BX1C). In Figure 7 we present the cloud compression and cooling efficiencies for the different B_x runs. We find that even a B_x field in initial equipartition with the thermal gas pressure has little influence on the compression or cooling of the cloud. A magnetic field component aligned with the direction of shock propagation thus appears to have little influence on the dynamic or thermal evolution of radiative clouds.

4.6. Effects of Numerical Resolution

Next we consider the effect of numerical resolution on our results. Run BY4C(L) uses an identical setup to run BY4C, but with half the resolution. Comparing these two runs gives us some idea of how well converged our solutions are. The high compression and efficient cooling in the B_y runs pose the most demanding resolution requirements of all the runs considered, so this example represents a worst case comparison of convergence.

Figure 6 includes a comparison of the cloud compression and cooling efficiencies as a function of time for these two runs. Although there is a significant time lag in the cooling and compression for run BY4C(L), the asymptotic values for the cloud compression and mass fraction cooled to $< 1000K$ generally agree well between the two runs ($\lesssim 10\%$ differences). The time lag can be attributed to the more diffusive nature of

low resolution grids, which tend to smear out concentrated density peaks and thereby increase the cooling times. This is particularly troublesome for low temperature coolants which generally require the resolution of much smaller spatial scales to capture the transition through the cooling plateau, and maintain their edge against thermalization effects arising from numerical viscosity.

We have already noted that many of our radiatively cooled runs reach a resolution limit toward the end of our simulations. This limit currently prevents us from reliably extending the duration of our simulations. Noting that the cold, dense cloud remnants occupy very few cells on the grid toward the ends of the simulations, it becomes clear that the most efficient approach to resolving the late-time evolution is to use an adaptive mesh scheme. This capability is currently being added to our code, and results will be presented in future work.

4.7. Effects of Artificial Resistivity

Finally we consider the role of reconnection in our results and compare the effectiveness of different numerical methods for dealing with it. We expect reconnection to be important whenever oppositely directed field lines come into close proximity. We note that this can not happen in our B_z runs since the field lines are prevented from bending or otherwise becoming oppositely directed by the enforced symmetry of our two-dimensional Cartesian geometry. For our B_x runs, reconnection is most likely to happen near the surface of the cloud, near the Mach stem downwind, or in any vortices that form. However, because most of these events are external to the cloud, we do not expect reconnection to play an important role in its evolution. Furthermore, we have already shown that B_x fields, in general, have little effect on the evolution of our cloud models, so it seems unlikely that reconnection would be important to our conclusions in that case. For our B_y runs, reconnection will be most important near the current sheet that forms along the symmetry plane downwind of the cloud (see panels E and F of Figure 1). When field lines on opposite sides of the current sheet are squeezed closer together than a zone width, numerical reconnection occurs and regions of the field transform into closed field loops, evident in panel F of Figure 1. The current sheet and reconnection events are also evident as very high β regions in panels E and F of Figure 2; β is high in these regions since reconnection events are characterized by the conversion of magnetic energy into thermal energy.

Clearly the way these reconnection events are handled numerically may have an effect on the final outcome of the simulations. As described in §3, Cosmos tracks reconnection through the use of a resistivity term designed to spread current sheets out so they are resolved and recapture any magnetic energy lost in reconnection through the internal energy equation. Up to this point all of the runs have used the Stone & Pringle (2001) form of resistivity η_{SP} with $k_1 = 0.1$ (equation 13). We now consider one run with $\eta = 0$ [run BY4C(L1)] and another using the Nitta et al. (2001) form η_N with $k_1 = 0.5$ (equation 14) [run BY4C(L2)]. Since we expect our B_y runs to be most affected by reconnection, we tailor these runs after run BY4C(L) from the previous section. Other than the form of η , these runs are all identical. We find that B_{max}/B_i , $\rho_{max}/\rho_{cl,i}$, and T_{min} are very similar in all three runs (Table 2), indicating that the form of artificial resistivity used has little impact on the cloud evolution during these runs. Differences between these runs are more evident in the downwind flow where, for instance, β_{min} varies by almost an order of magnitude.

5. Discussion and Summary

We have presented results from a series of two-dimensional shock-cloud simulations with the goal of highlighting the importance of different physical processes, including the interplay between hydrodynamic, radiative, and magnetic effects. These simulations represent the first such calculations we know of that simultaneously consider magnetic fields and radiative cooling. To facilitate easy comparison, we included runs with different combinations of physical processes active. We summarize our main results as follows:

1. Unmagnetized, non-radiative clouds are destroyed on a few dynamical timescales through hydrodynamic (Kelvin-Helmholtz and Rayleigh-Taylor) instabilities (Klein et al. 1994).
2. In the cooling-dominated regime, radiative clouds are *not* destroyed. Instead, they form dense, cold filaments, which are presumably the precursors to active star-forming regions (Mellema et al. 2002; Fragile et al. 2004).
3. Tension in magnetic field lines along the surface of a cloud can suppress the growth of hydrodynamic instabilities, thus increasing the cloud’s survivability even without radiative cooling (Mac Low et al. 1994; Jones et al. 1996). This is true for our external field cases (B_x and especially B_y) whenever the fields achieve sufficient strength ($\beta \lesssim 10^4$ to suppress Rayleigh-Taylor and $\beta \lesssim 0.02$ to suppress Kelvin-Helmholtz). On the other hand, internal fields that do not thread through the cloud surface (such as our B_z cases) are unable to suppress the growth of hydrodynamic instabilities.
4. External magnetic field lines that are stretched over the surface of a cloud can greatly enhance its compression. For radiative clouds, this can dramatically enhance the cooling efficiency. For instance, the fraction of cloud material cooling from 10^4 K to below 100 K increases from ~ 0.7 without magnetic fields (run C) to > 0.9 with a $\beta_0 = 4$, B_y field (run BY4C). This enhancement is negligible, however, for the B_x field orientation or an initially weak field aligned along B_y ($\beta_0 > 100$).
5. Internal magnetic field lines resist compression in a cloud. For radiative clouds, this can dramatically reduce the cooling efficiency. For instance, in simulations with a B_z field of only modest initial strength ($\beta_0 \lesssim 100$), the cloud material is prevented from cooling below 100 K. A very strong initial field ($\beta_0 \sim 1$) can even prevent cooling below 1000 K.

Obviously, the field configurations studied in this work are highly idealized. Real astrophysical fields are likely to have much more complex topologies (Vallée 2003). In particular, magnetic fields in galactic star-forming clouds are probably linked to underlying turbulent flow patterns (Mac Low & Klessen 2004). In that context, magnetic fields are important in stabilizing such clouds against collapse, a role similar to that of the *internal* fields in this work. However, those star-forming clouds are often very cold ($T < 100$ K) and subject to important physical process not considered in this work, such as neutral-ion drift, so we caution the reader against attempting to extrapolate our results to that regime.

Due to resolution requirements and computational limitations, the simulations in this work were carried out in two-dimensional Cartesian geometry, and so the clouds represent slices through infinite cylinders. This special geometry likely affects some of our conclusions. Here we speculate on how these results may change in three-dimensional simulations:

Since the initial compressive shock in the cloud is highly symmetric, the additional convergence expected in three-dimensional models might lead to stronger compressions and enhanced cooling in radiative clouds even without magnetic fields. Three-dimensional simulations would also provide an additional degree of freedom for fragmentation through dynamical instabilities.

The role of magnetic fields in three dimensions may be more complicated. For a spherical cloud, we lose the distinction between our B_y and B_z runs. Such transverse fields will cause enhanced compression of the cloud along one direction (the initial direction of the field), but will be unable to prevent expansion in the perpendicular direction. This lateral expansion can enhance the growth rate of the Rayleigh-Taylor instability (Gregori et al. 1999, 2000), an action that was prevented in this work by the assumed symmetry of the two-dimensional runs. Thus, in contrast to two-dimensional results, magnetic fields in three-dimensional simulations can hasten the destruction of non-radiative clouds. It remains to be seen how radiative cooling would modify this conclusion.

Self-gravity has been neglected in this study on account of the constrained cylindrical geometry. Although the cloud parameters are specifically chosen such that self-gravity is negligible initially, the local free-fall timescale becomes significantly shorter during the latter stages of compression. For the runs with radiative cooling active, self-gravity becomes important at approximately the time we stop the simulations. It would, therefore, be interesting to follow shock-cloud simulations in three-dimensions with radiative cooling, magnetic fields, and self-gravity included. To do this at comparable resolution to that used in this work will require the use of adaptive mesh refinement to concentrate resolution around the cloud fragments. Adaptive gridding is currently being added to the *Cosmos* code, and we plan to revisit this problem in future work.

The authors would like to thank the VisIt development team at Lawrence Livermore National Laboratory (<http://www.llnl.gov/visit/>), in particular Hank Childs and Akira Haddox, for visualization support. This work was performed under the auspices of the U.S. Department of Energy by University of California, Lawrence Livermore National Laboratory under Contract W-7405-Eng-48.

A. MHD Code Verification

Here we review some of the tests used to verify and validate the MHD coding of *Cosmos*. We consider transverse magnetic field pulse advection, circularly polarized Alfvén waves, sheared Alfvén waves, gas and magnetosonic rarefaction waves, MHD Riemann problems, and shock-cloud collisions. We do not discuss in detail the setup of any of these tests since they can all be found in the literature, which we reference where appropriate. The first test, the advection of transverse magnetic field pulses, yields field profiles identical to the van Leer results in Figure 1b of Stone et al. (1992) and we do not discuss this problem further. In the following paragraphs we summarize the results from each of the remaining tests.

To test the ability of *Cosmos* in handling smooth flows and to evaluate the convergence order of our methods, we consider the traveling circularly polarized Alfvén wave test from Tóth (2000). We calculate the mean-relative error (defined as $\bar{\epsilon}_{\text{rel}}^n(a) = \sum_{i,j,k} |a_{i,j,k}^n - A_{i,j,k}^n| / \sum_{i,j,k} |A_{i,j,k}^n|$, where $a_{i,j,k}^n$ and $A_{i,j,k}^n$ are the numerical and exact solutions, respectively) for B_{\perp} and v_{\perp} as a function of grid resolution (n). Here $B_{\perp} = B_y \cos \alpha - B_x \sin \alpha$ is the magnetic field component perpendicular to the direction of wave propagation, which is at an angle $\alpha = 30^{\circ}$ relative to the x axis. The perpendicular velocity component v_{\perp} is calculated similarly. For B_{\perp} we find errors $\bar{\epsilon}_{\text{rel}}^8(B_{\perp}) = 1.983$, $\bar{\epsilon}_{\text{rel}}^{16}(B_{\perp}) = 0.599$, $\bar{\epsilon}_{\text{rel}}^{32}(B_{\perp}) = 0.133$, and $\bar{\epsilon}_{\text{rel}}^{64}(B_{\perp}) = 0.033$. For v_{\perp} we find errors $\bar{\epsilon}_{\text{rel}}^8(v_{\perp}) = 0.985$, $\bar{\epsilon}_{\text{rel}}^{16}(v_{\perp}) = 0.369$, $\bar{\epsilon}_{\text{rel}}^{32}(v_{\perp}) = 0.114$, and $\bar{\epsilon}_{\text{rel}}^{64}(v_{\perp}) = 0.041$. The averages of our errors at each resolution are similar to the averages reported in Tóth (2000) for the Flux-CD/CT scheme. The errors converge at approximately second order.

Figure 18 in Stone et al. (1992) clearly demonstrates the need to test thoroughly the limit of sheared Alfvén wave propagation, which can generate unacceptable levels of dispersive error. This class of tests has led to the development of a more stable method of characteristics to compute properly centered electromotive and Lorentz forces. We adopt a similar approach here and use the Alfvén characteristic equation to estimate causal interpolants and predict time-averaged estimates of the magnetic and velocity fields used as sources in the transverse components of equations (10) and (12), in particular the $(\mathbf{B} \cdot \nabla)\mathbf{B}$ and $(\mathbf{B} \cdot \nabla)\mathbf{v}$ terms. Our results are identical to Figures 18 and 19 of Stone et al. (1992) for the two cases in which we use conventional differencing and the method of characteristics, respectively.

The ability of *Cosmos* to capture and propagate nonlinear waves and shocks is evaluated with the MHD analog of the classic Sod shock tube problem of hydrodynamics introduced by Brie & Wu (1988). Since there is no known analytic solution for this problem, we test the convergence of our numerical solutions using a self-convergence test. For two successive runs with a resolution ratio of two, we calculate the L_1 norm error (i.e., $L_1^n(a) = \sum_{i,j,k} \Delta x_i \Delta y_j \Delta z_k |a_{i,j,k}^n - a_{i,j,k}^{2n}|$, where $a_{i,j,k}^n$ and $a_{i,j,k}^{2n}$ are the numerical solutions for n and $2n$ zones, respectively, and $j = k = \Delta y_j = \Delta z_k = 1$ for this 1D problem). For the fluid density we find errors $L_1^{64}(\rho) = 0.00691$, $L_1^{128}(\rho) = 0.00362$, $L_1^{256}(\rho) = 0.00211$, and $L_1^{512}(\rho) = 0.00127$. As expected for shock problems, the convergence is approximately first order, and our results are similar to Stone et al. (1992).

For certain one-dimensional problems, Falle (2002) reported significant errors when using the publically available ZEUS MHD code. Since *Cosmos*, as applied in this work, uses a ZEUS-like MHD scheme, we give particular emphasis to investigating these problems. Our results show that *Cosmos* performs significantly better than the version of ZEUS used in Falle (2002), due in part to the introduction of artificial resistivity. To illustrate this, in Figures 8 and 9, we show the *Cosmos* results when applied to the fast rarefaction and Riemann test problems from Figures 2 and 6 of Falle (2002). In each figure, we include results with both the Stone & Pringle (2001) and Nitta et al. (2001) forms of artificial resistivity and with no artificial resistivity ($\eta = 0$). The resistivity coefficient is set to $k_1 = 0.5$ for the fast rarefaction and $k_1 = 1.0$ for the Riemann problem. In both problems, the Courant factor is set to 0.5, and the linear and quadratic artificial viscosity

coefficients are set to 0.2 and 2.0, respectively. For the fast rarefaction, Cosmos performs much better than the ZEUS results shown in Falte (2002). Furthermore, we note that Cosmos is also less diffusive than the upwind method employed in Falte (2002) when either no resistivity or the Stone & Pringle (2001) form of resistivity are used. When the Nitta et al. (2001) form is used, our results appear similar to the upwind method. Cosmos also significantly outperforms the ZEUS code on the Riemann problem and successfully captures all of the features, due predominately to the addition of artificial resistivity. On this problem, the Nitta et al. (2001) form of resistivity yields better results. Next, we consider the smooth gas rarefaction and stationary shock problems from Figures 3 and 5 of Falte (2002). For the smooth gas rarefaction, Falte (2002) noted that, despite being a second-order code, ZEUS yields only first-order convergence. For Cosmos, we find errors of $\bar{\epsilon}_{\text{rel}}^{50}(\rho) = 1.4 \times 10^{-2}$, $\bar{\epsilon}_{\text{rel}}^{100}(\rho) = 3.8 \times 10^{-3}$, $\bar{\epsilon}_{\text{rel}}^{200}(\rho) = 9.2 \times 10^{-4}$, $\bar{\epsilon}_{\text{rel}}^{400}(\rho) = 2.7 \times 10^{-4}$, and $\bar{\epsilon}_{\text{rel}}^{800}(\rho) = 8.4 \times 10^{-5}$, which converge at approximately second order, as expected. On the stationary shock problem, although Cosmos does not achieve the same level of accuracy as the upwind code employed in Falte (2002), the error in Cosmos as measured from the analytical post-shock gas pressure plateau is about three times smaller than for ZEUS. This, again, is attributed mostly to the addition of artificial resistivity.

For our final test we simulate the magnetized shock-cloud collision first described in Dai & Woodward (1998) and repeated in Tóth (2000). This test is particularly appropriate for the investigations considered in this work. We investigate this problem using an $n \times n$ grid with $n = 50, 100, 200$, and 400 . The mean-relative errors in density and B^2 as a function of resolution are $\bar{\epsilon}_{\text{rel}}^{50}(\rho) = 0.103$, $\bar{\epsilon}_{\text{rel}}^{50}(B^2) = 0.283$, $\bar{\epsilon}_{\text{rel}}^{100}(\rho) = 0.061$, $\bar{\epsilon}_{\text{rel}}^{100}(B^2) = 0.186$, $\bar{\epsilon}_{\text{rel}}^{200}(\rho) = 0.030$, and $\bar{\epsilon}_{\text{rel}}^{200}(B^2) = 0.086$, where we have used the high-resolution (400×400 zone) simulation as the reference solution. Again the convergence is approximately first order as expected for this type of problem, and our errors are consistent with those reported by Tóth (2000).

REFERENCES

Anninos, P., & Fragile, P. C. 2003, *ApJS*, 144, 243

Anninos, P., Fragile, P. C., & Murray, S. D. 2003, *ApJS*, 147, 177

Begelman, M. C., & Cioffi, D. F. 1989, *ApJ*, 345, L21

Blanco, V. M., Graham, J. A., Lasker, B. M., & Osmer, P. S. 1975, *ApJ*, 198, L63

Brackbill, J. U., & Barnes, D. C. 1980, *J. Comp. Phys.*, 35, 426

Brie, M., & Wu, C. C. 1988, *J. Comp. Phys.*, 75, 400

Chambers, K. C., Miley, G. K., & van Breugel, W. 1987, *Nature*, 329, 604

Chandrasekhar, S. 1961, *Hydrodynamic and hydromagnetic stability* (International Series of Monographs on Physics, Oxford: Clarendon, 1961)

Dai, W., & Woodward, P. R. 1998, *J. Comp. Phys.*, 142, 331

De Young, D. S. 1989, *ApJ*, 342, L59

Dedner, A., Kemm, F., Kröner, D., Munz, C. D., Schnitzer, T., & Wesenberg, M. 2002, *J. Comp. Phys.*, 175, 645

Falle, S. A. E. G. 2002, *ApJ*, 577, L123

Field, G. B. 1965, *ApJ*, 142, 531

Fitt, A. J., & Alexander, P. 1993, *MNRAS*, 261, 445

Fragile, P. C., Murray, S. D., Anninos, P., & van Breugel, W. 2004, *ApJ*, 604, 74

Gregori, G., Miniati, F., Ryu, D., & Jones, T. W. 1999, *ApJ*, 527, L113

Gregori, G., Miniati, F., Ryu, D., & Jones, T. W. 2000, *ApJ*, 543, 775

Jones, T. W., Ryu, D., & Tregillis, I. L. 1996, *ApJ*, 473, 365

Kahn, F. D. 1976, *A&A*, 50, 145

Klein, R. I., McKee, C. F., & Colella, P. 1994, *ApJ*, 420, 213

Krause, M., & Löhr, A. 2004, *A&A*, 420, 115

Mac Low, M., & Klessen, R. S. 2004, *Reviews of Modern Physics*, 76, 125

Mac Low, M., McKee, C. F., Klein, R. I., Stone, J. M., & Norman, M. L. 1994, *ApJ*, 433, 757

Magara, T., Shibata, K., & Yokoyama, T. 1997, *ApJ*, 487, 437

McCarthy, P. J. 1993, *ARA&A*, 31, 639

McCarthy, P. J., van Breugel, W., Spinrad, H., & Djorgovski, S. 1987, *ApJ*, 321, L29

McKee, C. F., & Hollenbach, D. J. 1980, *ARA&A*, 18, 219

Mellema, G., Kurk, J. D., & Röttgering, H. J. A. 2002, A&A, 395, L13

Murray, S. D., & Lin, D. N. C. 1989, ApJ, 339, 933

Nitta, S., Tanuma, S., Shibata, K., & Maezawa, K. 2001, ApJ, 550, 1119

Nittman, J. 1981, MNRAS, 197, 699

Rand, R. J., & Kulkarni, S. R. 1989, ApJ, 343, 760

Rees, M. J. 1989, MNRAS, 239, 1P

Stone, J. M., Hawley, J. F., Evans, C. R., & Norman, M. L. 1992, ApJ, 388, 415

Stone, J. M., & Pringle, J. E. 2001, MNRAS, 322, 461

Tóth, G. 2000, J. Comp. Phys., 161, 605

Vallée, J. P. 2003, New Astronomy Review, 47, 85

van Breugel, W., Filippenko, A. V., Heckman, T., & Miley, G. 1985, ApJ, 293, 83

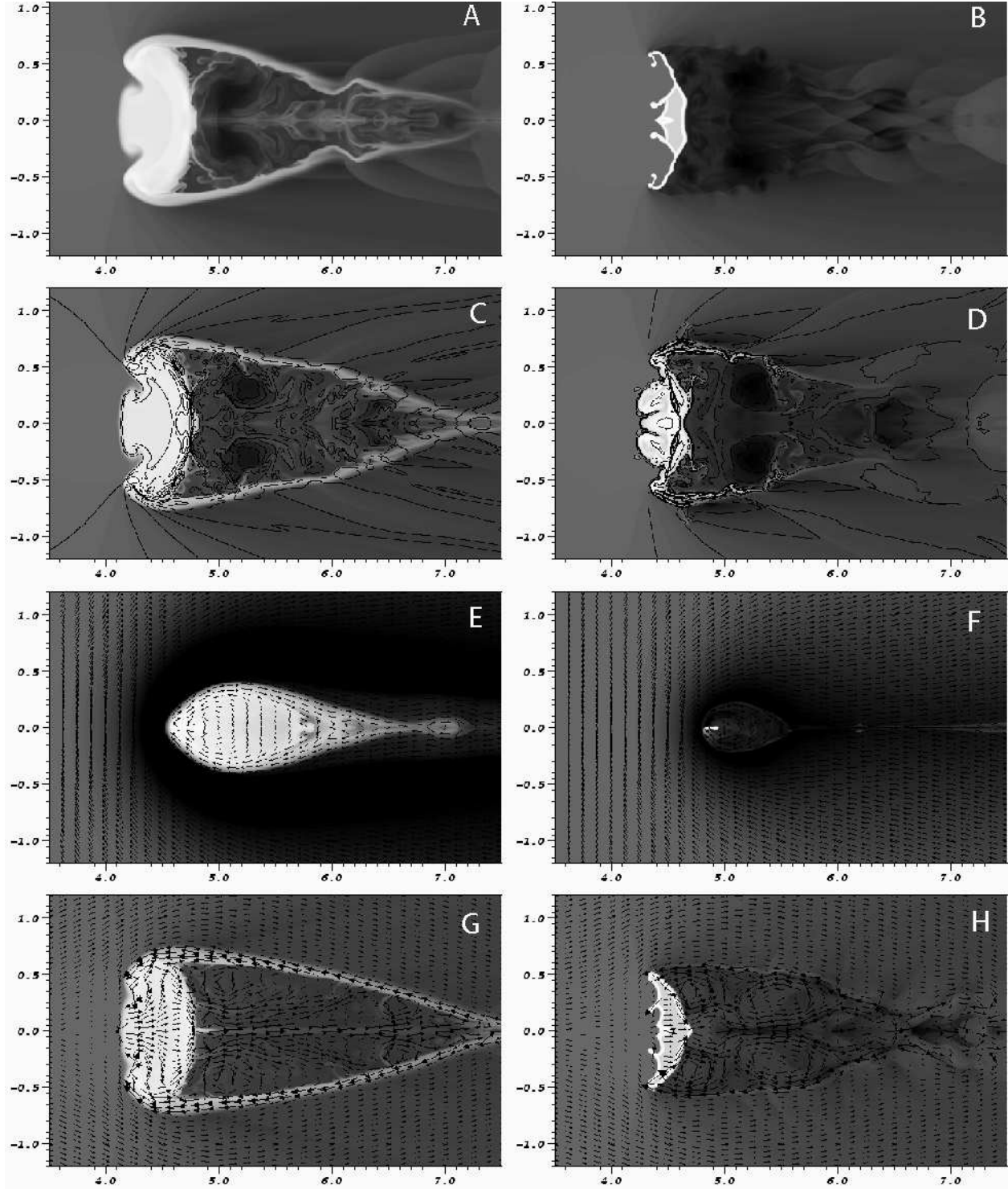


Fig. 1.— Grayscale contour plots of $\log(\rho)$ for runs A (panel A), C (panel B), BZ4A (panel C), BZ4C (panel D), BY4A (panel E), BY4C (panel F), BX4A (panel G) and BX4C (panel H) at time $t = t_{cc}$. For runs BZ4A and BZ4C we include contours of $\log(B^2/8\pi)$. For runs BY4A, BY4C, BX4A, and BX4C we include a sampling of logarithmically-scaled arrows representing the local magnetic field; these arrows are scaled separately for each figure.

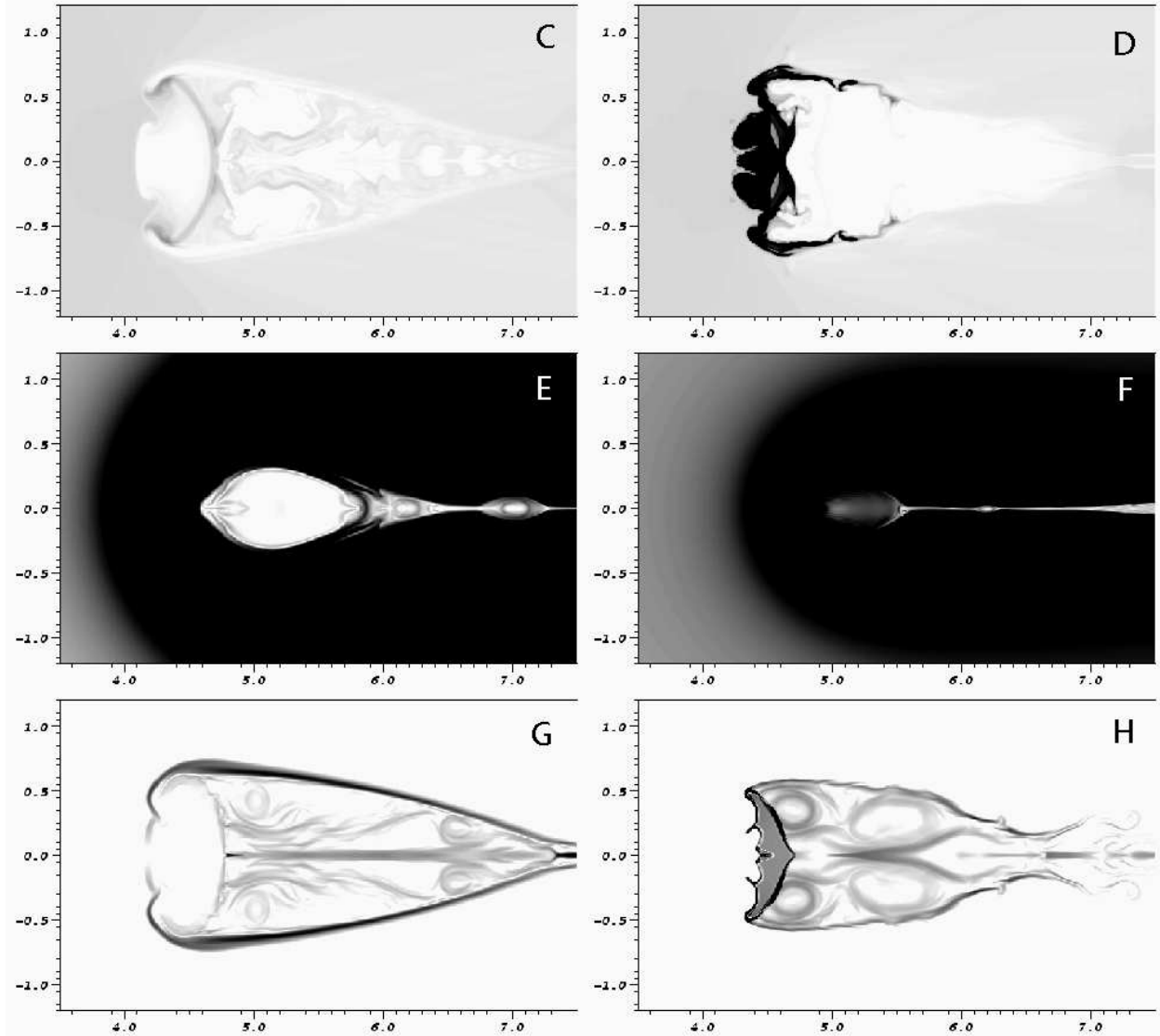


Fig. 2.— Grayscale contour plots of $\log(\beta)$ for runs BZ4A (panel C), BZ4C (panel D), BY4A (panel E), BY4C (panel F), BX4A (panel G), and BX4C (panel H) at time $t = t_{cc}$. The scale of the plot goes from $\beta = 0.1$ (black) to $\beta = 100$ (white).

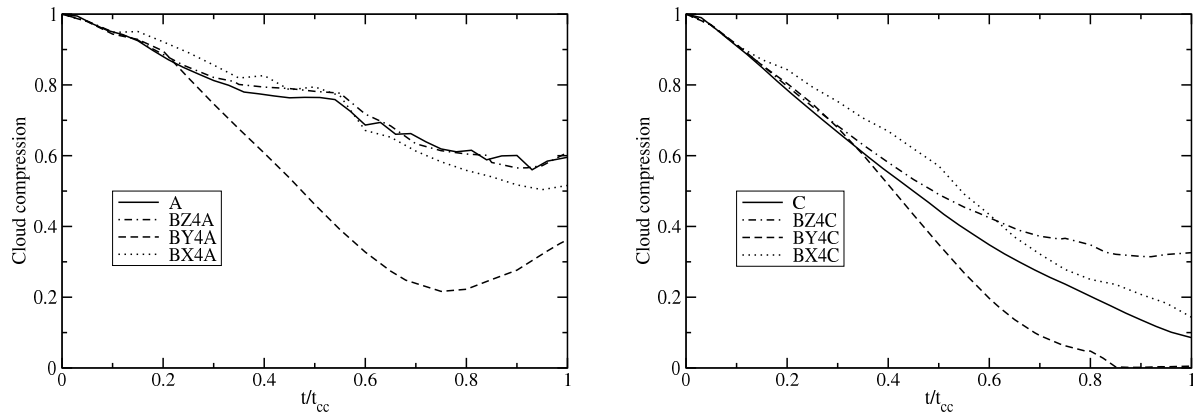


Fig. 3.— Plot of cloud compression (ζ) as a function of time for (a) the non-radiative runs (A, BZ4A, BY4A, and BX4A) and (b) the radiatively-cooled runs (C, BZ4C, BY4C, and BX4C).

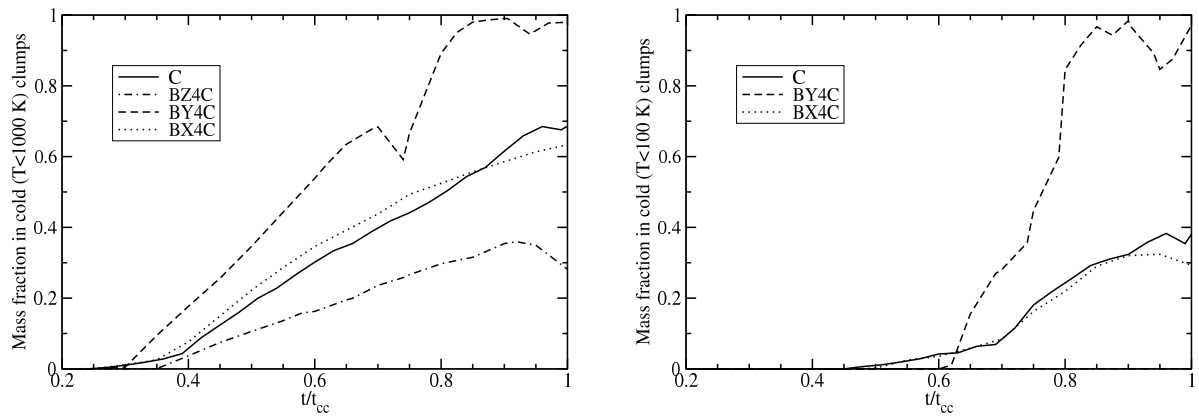


Fig. 4.— Fraction of initial cloud material that has cooled below (a) $T = 1000$ K and (b) $T = 100$ K as a function of time for runs C, BZ4C, BY4C, and BX4C. Note that in run BZ4C none of the cloud material cools below $T = 100$ K.

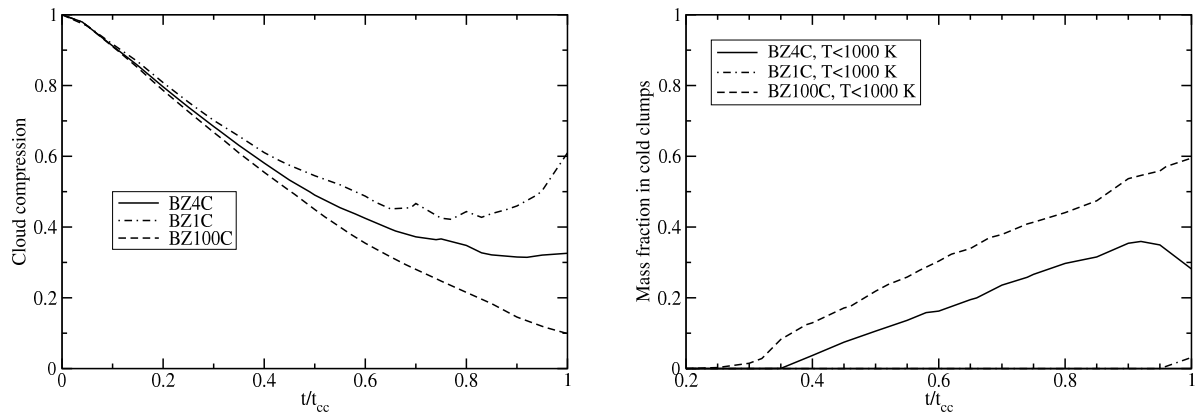


Fig. 5.— Comparison of cloud compression (a) and cooling efficiency (b) for the radiatively-cooled B_z runs.

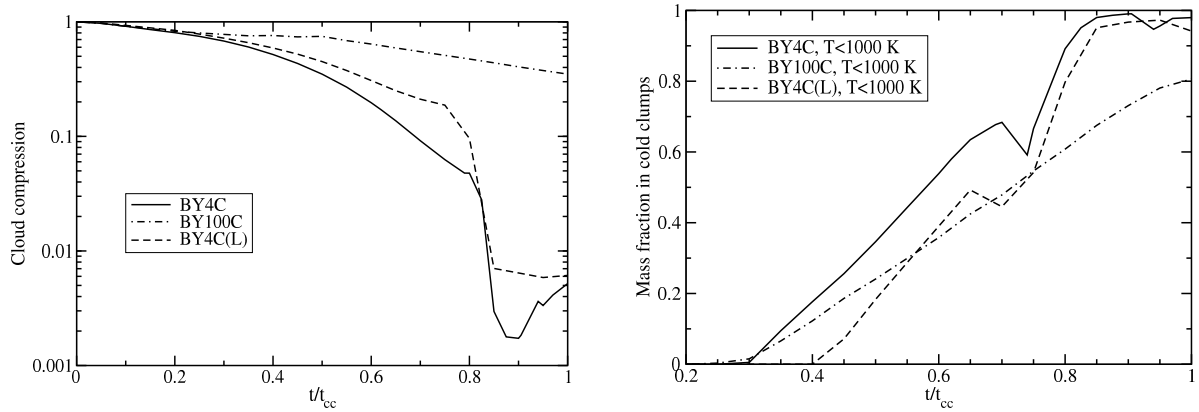


Fig. 6.— Comparison of cloud compression (a) and cooling efficiency (b) for the radiatively-cooled B_y runs.

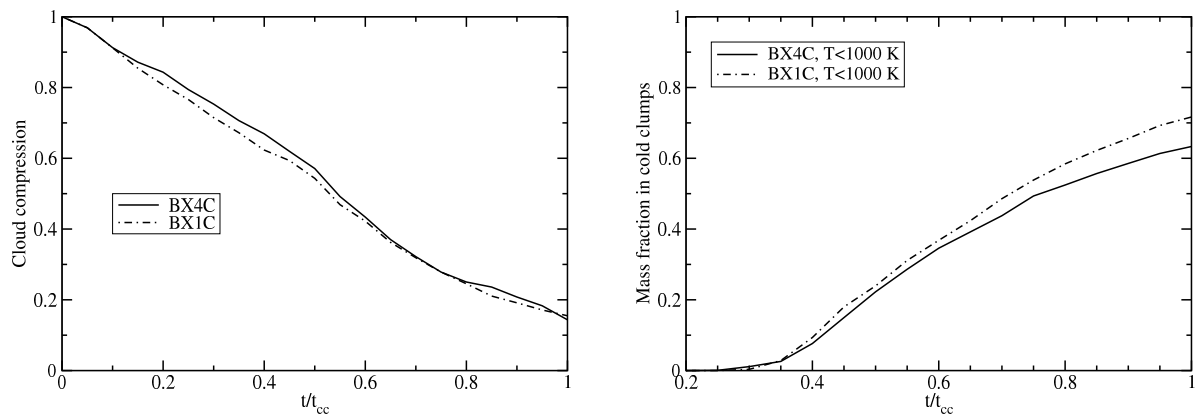


Fig. 7.— Comparison of cloud compression (a) and cooling efficiency (b) for the radiatively-cooled B_x runs.

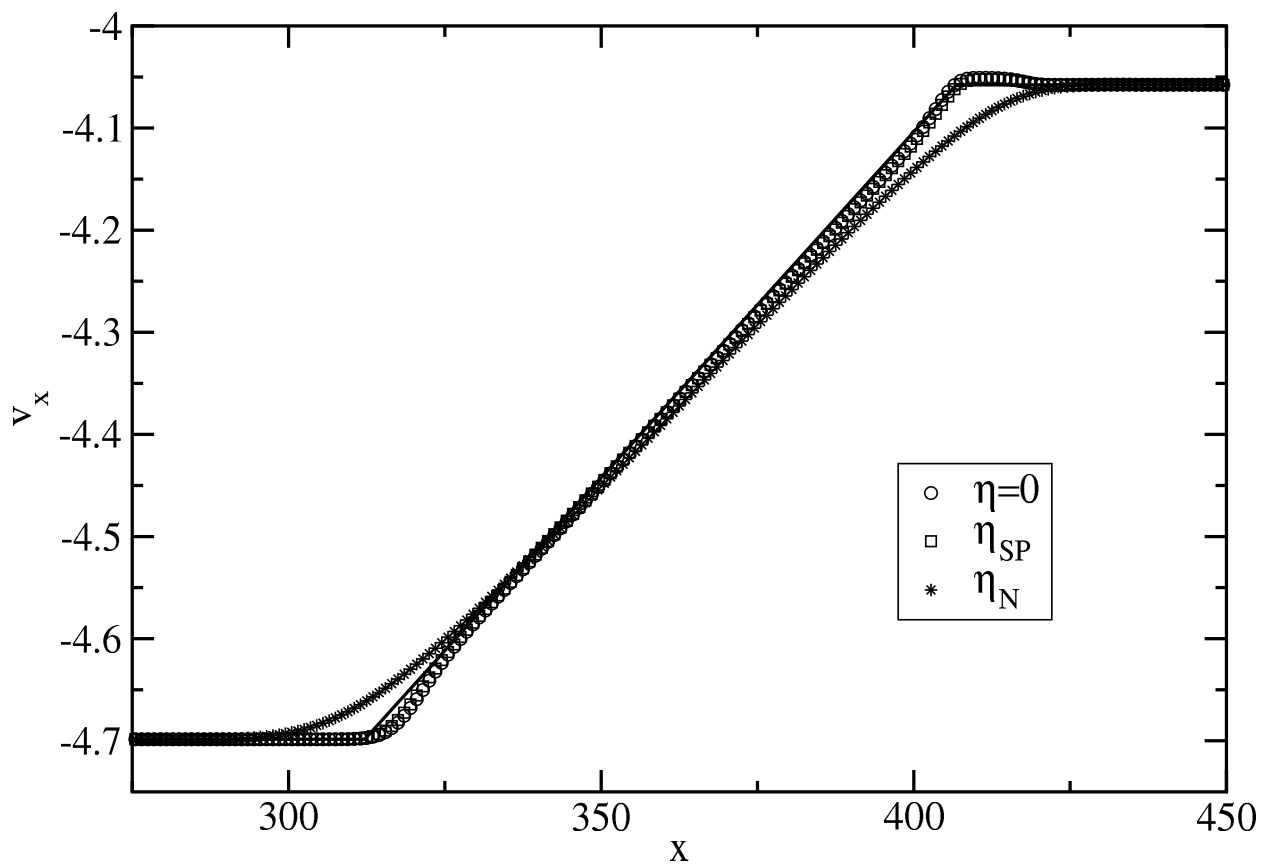


Fig. 8.— Test of the fast rarefaction wave from Figure 2 of Falle (2002), comparing results using different forms of artificial resistivity. The solid line gives the exact solution for this problem.

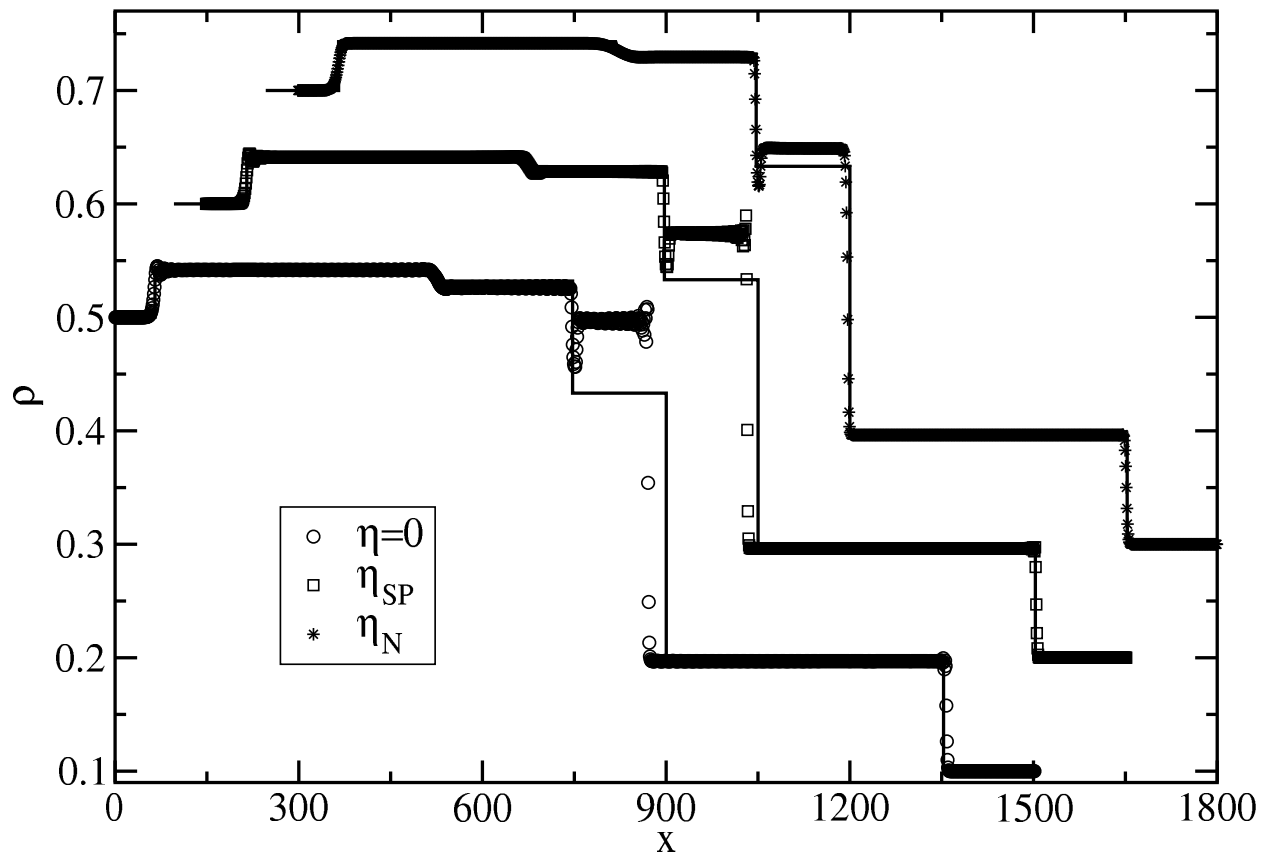


Fig. 9.— Test of the Riemann problem from Figure 6 of Falle (2002), comparing results using different forms of artificial resistivity. The solid lines give the exact solution for this problem. The results are offset for clarity.

Table 1. Model Parameters

Run	Resolution ^a	β_0	Field Component	Cooling
A	200	∞		no
C	200	∞		yes
BZ4A	200	4	B_z	no
BZ4C	200	4	B_z	yes
BY4A	200	4	B_y	no
BY4C	200	4	B_y	yes
BX4A	200	4	B_x	no
BX4C	200	4	B_x	yes
BZ1C	200	1	B_z	yes
BZ100C	200	100	B_z	yes
BY100C	200	100	B_y	yes
BX1C	200	1	B_x	yes
BY4C(L)	100	4	B_y	yes
BY4C(L1)	100	4	B_y	yes
BY4C(L2)	100	4	B_y	yes

^aInitial number of zones per cloud radius.

Table 2. Summary of Key Results at $t = t_{cc}$

Run	β_{min}	B_{max}/B_i	$\rho_{max}/\rho_{cl,i}$	T_{min} (K)
A	1.5E1	5.3E4
C	8.7E2	2.4E1
BZ4A	4.1	1.3E1	1.3E1	4.4E4
BZ4C	1.9E-3	7.3E1	4.7E1	3.8E2
BY4A	1.6E-5	1.8E2	4.7E1	2.8E5
BY4C	3.8E-5	8.2E2	2.1E4	1.5E1
BX4A	2.9E-1	2.5E1	1.1E1	6.1E4
BX4C	4.0E-3	3.9E1	7.2E2	2.6E1
BZ1C	7.1E-4	4.2E1	4.2E1	3.0E2
BZ100C	1.1E-3	3.4E2	1.3E2	1.0E2
BY100C	5.4E-6	5.7E2	1.5E3	2.2E1
BX1C	3.7E-3	1.9E1	1.0E3	2.3E1
BY4C(L)	2.8E-5	4.7E2	5.4E3	1.8E1
BY4C(L1)	6.9E-5	4.8E2	4.4E3	1.9E1
BY4C(L2)	1.1E-4	4.3E2	5.9E3	2.2E1